NONSYMMETRIC BRANCHING OF FLUID FLOWS IN 3D VESSELS

N. C. OVENDEN[✉1] and F. T. SMITH[1]

Abstract

Nonsymmetric branching flow through a three-dimensional (3D) vessel is considered at medium-to-high flow rates. The branching is from one mother vessel to two or more daughter vessels downstream, with laminar steady or unsteady conditions assumed. The inherent 3D nonsymmetry is due to the branching shapes themselves, or the differences in the end pressures in the daughter vessels, or the incident velocity profiles in the mother. Computations based on lattice-Boltzmann methodology are described first. A subsequent analysis focuses on small 3D disturbances and increased Reynolds numbers. This reduces the 3D problem to a two-dimensional one at the outer wall in all pressure-driven cases. As well as having broader implications for feeding into a network of vessels, the findings enable predictions of how much swirling motion in the cross-plane is generated in a daughter vessel downstream of a 3D branch junction, and the significant alterations provoked locally in the shear stresses and pressures at the walls. Nonuniform incident wall-shear and unsteady effects are examined. A universal asymptotic form is found for the flux change into each daughter vessel in a 3D branching of arbitrary cross-section with a thin divider.

1. Introduction

Branch-junction sites are medically important for flow blockage and disease initiation [3, 4, 13, 26–28, 32]. They significantly influence cardiovascular performance in the human torso and cerebrovascular effects in the head. The need to increase understanding of angiogenesis has prompted much work [16, 23, 30] on arterial and similar networks and their evolution. For example, a principal cause of haemorrhagic stroke is cerebral arteriovenous malformations [2, 19, 22, 39, 42], where one upstream vessel (mother) typically supplies incident blood flow to many downstream vessels (daughters) instead of just the conventional two downstream vessels. Additionally, reconnections can occur in which many daughter vessels merge

---

[1]Department of Mathematics, University College London, Gower St, London WC1E 6BT, UK;
e-mail: n.ovenden@ucl.ac.uk, f.smith@ucl.ac.uk.

further downstream into a few grand-daughter vessels. Our continued research here, which springs from long-term collaborations with clinicians at the National Hospital for Neurology and Neurosurgery, Queen Square, London, UK, is based on the key role of branch junctions in haemodynamical modelling.

In this paper, our interest is in specific applied mathematical questions that have arisen from consideration of the physiological issues. The questions, which are difficult and not previously addressed, we believe are fundamental to understanding the three-dimensional (3D) flows present and to appreciation of the flow structure. They centre on trends at increased flow rates. We do not claim direct application to the physiological flows mentioned, neither are we concerned with direct numerical solutions alone, which have been and continue to be done well by other researchers for particular flow rates, divergence angles and so on. Instead, our central focus is on theoretical/analytical approaches as described above. This focus is supplemented by the expectation that any significant results or trends that emerge are likely to apply to almost any cross-sectional shape of vessel.

Internal fluid motions through branch junctions in vessels have traditionally been studied by means of theory, mostly applied to ideal two-dimensional (2D) geometries and corresponding planar flows. Some main examples [11, 17, 24, 40] are on one-to-two branchings or bifurcations from one mother vessel to two daughter vessels, and on one-to-many branchings from one mother to many daughters [33, 34, 36]. In addition, a comparatively small number of investigations for symmetric 3D bifurcations have been pursued [6, 8, 25, 31, 33, 36, 37]. There, the symmetry refers not only to the mother vessel shape in cross section, but also to the daughter shapes and their associated flows being mutual mirror images with respect to the appropriate symmetry plane. Relatively simple symmetric branching models have also been used in developing descriptions of network flows through connected vessels [9], motivated by possible applications to cardiovascular, lung and cranial fluid dynamics, as well as in a variety of industrial settings.

It is clear then that most previous theoretical studies exclude the extra complexity associated with nonsymmetry in 3D branching flows. The only exceptions appear to be for low flow rates [38] and for a side-branching [35] at medium-to-high flow rates. Yet, in reality and in experiments [14, 15, 29], 3D nonsymmetry is the most common case of all the types of branching encountered. This is certainly the case throughout the human circulation system, including both the trunk and the brain. This observed 3D nonsymmetry can be caused by unequal pressures at the downstream ends of the daughter vessels, by the branching geometry itself, or by the incident velocity profiles in the mother being nonsymmetric. There are many other important specific influences such as the area ratios [5, 6, 8, 25, 31, 34, 36, 37], divergence angles, wall roughness, wall flexibility, the number of daughter vessels and unsteadiness, although it is noted that flow pulsatility is less significant in the cerebrovasculature beyond the circle of Willis.

Nonsymmetry in 3D poses severe theoretical difficulties. There is also some difficulty in 2D nonsymmetry, but it is far less severe [24]. In 3D (unlike in 2D) it is not

known in advance, for instance, what amount of swirl emerges in the motion within a daughter vessel downstream of any branch junction. Such lack of prior knowledge tends to rule out the very arguments on mass and momentum balancing that can be easily exploited analytically in 2D [5, 33, 34, 36]. In fact, little or no analytical work on the subject of 3D nonsymmetric branching flows at medium-to-high flow rates has been done as far as we know. Tadjfar and Smith [37] offer some promise based on the use of small-angle theory. Their theoretical results, for a single mother flow through a tube of circular cross-section dividing into two divergent daughters, are found to agree reasonably closely with direct simulations for angles of divergence up to 120 degrees. Thus, a surprisingly wide range of divergence angles seems to be covered by the theory, over a range of medium flow rates with Reynolds numbers in the low hundreds typically. Characteristic Reynolds numbers of practical/biomedical interest are also in the hundreds and divergence angles in reality are extremely varied [37]. Yet more guidance from direct computations could be helpful for insight into other fundamental settings.

The current investigation into fundamental 3D nonsymmetric branching motions combines computational and analytical contributions along with comparisons between them. The computational contribution uses a lattice-Boltzmann approach [20, 41] to simulate an incompressible flow driven by a pressure gradient through a branching structure and is able to provide some insight into nonsymmetric effects over a range of flow rates. The analytical contribution is concerned mainly with small disturbances and medium-to-high Reynolds numbers. This is partly because such disturbances seem to be the obvious first ones to address, and the above computations suggest their usefulness could persist over a surprisingly broad range of flow conditions. In the analytical investigation, the end pressures are assumed to apply over a relatively short axial length scale comparable with the representative tube diameter, and they are prescribed whereas in a fuller system they would be related to the long-scale pressure differences as in previous works [31, 37]. Shape effects and others can be likewise considered over the same axial length scale. The one-to-two and one-to-many cases of branching as before are both of major biomedical interest.

Section 2 describes the branching-flow configuration. The motion is taken to be laminar, steady or unsteady, but with three-dimensionality and nonsymmetry throughout, and the contained fluid is taken to be incompressible. Section 3 then presents the numerical methodology and some results, leading on to the analysis in Section 4. The crucial influence of the incoming velocity profile in the mother tube is felt through a normalized wall-shear distribution, $\lambda(s)$, where s is the distance measured tangentially to the wall in the cross-sectional plane. Steady pressure-driven flows with two or more daughter tubes are considered first in Section 4. These pressure-driven flow analyses show how pressure differences can be sustained within a short length scale in the neighbourhood of a 3D branch junction, an important aspect for network modelling which has to deal with all length scales in effect. Section 4 also considers shape-driven flows and corner vortices. Comparisons between computation and analysis are given in Section 5. The influence of a nonuniform $\lambda(s)$ distribution
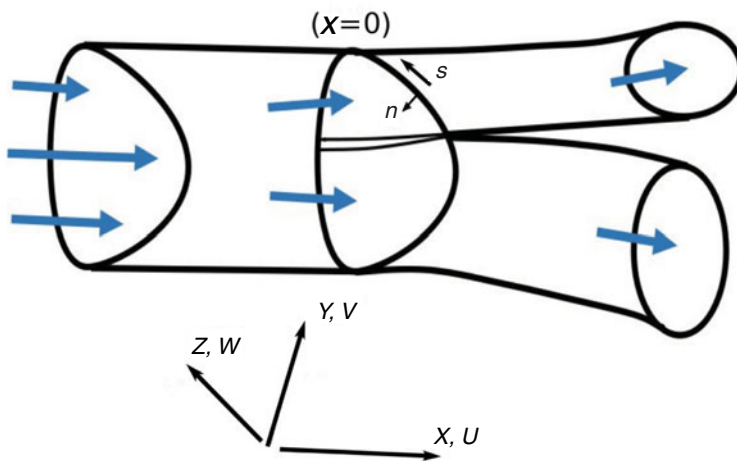
FIGURE 1. Schematic diagram of the 3D branching flow configuration from one mother tube to two daughter tubes, in nondimensional terms. Length scales are broadly $O(1)$ in x, y, z and the velocities u, v and w are also typically $O(1)$. More daughter vessels are also considered in the paper.

is then discussed in Section 6, and unsteady flows are investigated in Section 7. Conclusions, including final comments, are made in Section 8.

2. Branching-flow configuration

The branching configuration is shown schematically in Figure 1 for a one-to-two case. The length scales of concern include those comparable with the typical tube cross-sectional distance a_D, where the subscript D denotes a dimensional quantity. The lengths, velocities, pressure and time to be used here are nondimensionalized with respect to a_D, u_D, $\rho_D u_D^2$, a_D/u_D in turn, where u_D is a representative velocity in the incident flow and ρ_D is the density of the incompressible fluid. In nondimensional Cartesian terms, the axial coordinates and velocities in the mother tube are x and u, respectively, while those in the cross-plane are y, v and z, w; the pressure variation is p and the time is denoted by t. For convenience, we will also use s and n as corresponding orthogonal nondimensional coordinates which are tangential and (inwardly) normal to the outer walls, respectively, in the cross-plane.

The Reynolds number Re is $a_D u_D/\nu_D$, where ν_D is the kinematic viscosity. Ahead of the branch junction, where x is negative, the incident cross-sectional profile of the mother tube is taken to be of a general smooth shape; its contained forward-flow velocity profile may be a fully developed one but, in any case, it has a positive normalized wall-shear distribution $\lambda(s)$, that is, $\partial u/\partial n$ at the wall, which could depend on the position s around the outer wall.

3. Lattice-Boltzmann computations and results

Lattice-Boltzmann methods are based on kinetic theory and solve a discretized version of the Boltzmann equation computed on a lattice [1, 12, 41]. It is possible to show via the so-called Chapman–Enskog asymptotic expansion (in orders of the Knudsen number) [20, 41] that the solution to the standard lattice-Boltzmann approach represents a weakly compressible approximation to the incompressible Navier–Stokes equation with an error comparable to the square of the Mach number. Since its appearance 30 years ago, the simple formulation of the lattice-Boltzmann approach with local update rules based on particle interactions, coupled with its remarkable scalability for parallel processing systems, have led to it becoming a popular alternative numerical scheme for fluid dynamics problems. Its weakly compressible nature means that the pressure satisfies an equation of state and therefore, unlike solving the incompressible Navier–Stokes equations, special numerical treatments are not required to solve a Poisson-type problem to obtain the pressure variations across the domain. Lattice-Boltzmann approaches are also ideally suited to multiphase flow and particle suspensions, the physics of which are vitally important in many aspects of physiological fluid dynamics [1].

The basic equation solved by our numerical simulation is

$$\frac{\partial F_i}{\partial t} + \mathbf{c}_i \cdot \nabla F_i = -\frac{1}{\tau}(F_i - F_i^{\text{eq}}) \quad \text{for } i = 1, \ldots, N,$$

where $\mathbf{c}_i$ are a finite set of N velocities, with associated distribution functions $F_i(\mathbf{x}, t)$ that describe the statistical distribution of gas particles. The collision operator on the right-hand side assumes that the Bhatnagar, Gross and Krook approximation holds [7, 12], where τ is the relaxation time and F_i^{eq} is the local Maxwellian distribution [41] based on the maximum entropy principle. To compute an internal fluid flow, a 3D regular lattice must be adopted with an associated finite set of velocities. For our simulations, the D3Q19 lattice was chosen [41] which has 19 distribution functions, F_i, each associated with one of the following velocities: $\mathbf{c}_0 = (0, 0, 0)$, $\mathbf{c}_{1,2} = (\pm 1, 0, 0)$, $\mathbf{c}_{3,4} = (0, \pm 1, 0)$, $\mathbf{c}_{5,6} = (0, 0, \pm 1)$ and $\mathbf{c}_{7,8,9,10} = (\pm 1, \pm 1, 0)$, $\mathbf{c}_{11,12,13,14} = (\pm 1, 0, \pm 1)$, $\mathbf{c}_{15,16,17,18} = (0, \pm 1, \pm 1)$. Internal and external lattice points are then defined on adopting a branching geometry of interest and, by nondimensionalizing the Boltzmann equation based on a characteristic length scale, typical flow speed and advection time, the lattice-Boltzmann model can be solved by a simple internal streaming process of the form:

$$F_i(\mathbf{x} + \mathbf{c_i}\Delta t, t + \Delta t) = F_i(\mathbf{x}, t)(1 - \omega) + \omega F_i^{(\text{eq})}, \tag{3.1}$$

where $\omega = \Delta t/\tau$ is the so-called collision frequency. By carefully choosing the nondimensional Δt to be the Knudsen number, the distributions $i \neq 0$ are updated and propagated at each time step along the relevant characteristic to their nearest neighbour lattice point. The collision frequency ω is related to the effective kinematic viscosity ν by the relation $\nu = (\omega^{-1} - 1/2)/3$, and, thus, ω represents a tunable parameter that can be used to vary the internal Reynolds number, Re, of the flow. In our simulations,
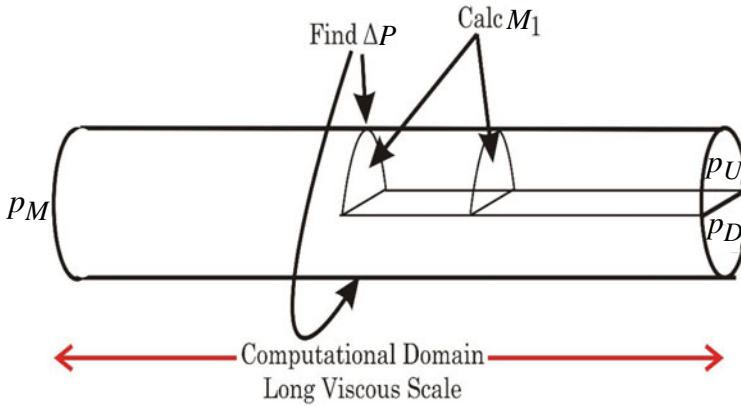
FIGURE 2. Typical branching geometry used in the lattice-Boltzmann simulations.

an exact incompressible scheme, initially proposed by He and Luo [20], is used for computing steady flow fields where the pressure $p(\mathbf{x}, t)$ and macroscopic velocity field $\mathbf{u}(\mathbf{x}, t)$ can be recovered from the distribution functions via the relations

$$p(\mathbf{x}, t) = \sum_i F_i(\mathbf{x}, t) \quad \text{and} \quad \mathbf{u}(\mathbf{x}, t) = \sum_i \mathbf{c}_i F_i(\mathbf{x}, t).$$

Finally, the local Maxwellian distribution needed to close the model is given by

$$F_i^{(\text{eq})}(\rho, \mathbf{u}) = \mathcal{W}_i[p + 3\mathbf{c_i} \cdot \mathbf{u} + \tfrac{9}{2}(\mathbf{c_i} \cdot \mathbf{u})^2 - \tfrac{3}{2}\mathbf{u}^2],$$

with the weights for the D3Q19 lattice being $\mathcal{W}_0 = 1/3$, $\mathcal{W}_{1-6} = 1/18$ and $\mathcal{W}_{7-18} = 1/36$.

Figure 2 shows the typical branching vessel geometry and computational domain used in the lattice-Boltzmann simulations presented here. Boundary conditions such as no-slip are relatively straightforward to implement in the lattice-Boltzmann approach; indeed, one of the advantages of this methodology is its ability to model flow in complex irregular geometries. For the typical cylindrical branching geometries studied here, second-order accuracy for curved boundaries is needed and, therefore, the no-slip condition proposed by Guo et al. [18] is used in our simulations. To generate a nonsymmetric flow field through the branching geometry, different end pressures, p_M, p_U and p_D, are maintained on the long viscous scale where the incoming distributions are determined using a method modified from that proposed by Inamuro et al. [21] for wall conditions. For a steady flow field, the lattice-Boltzmann iteration of updating and propagating the distribution functions across the lattice is repeated until unchanging macroscopic velocity and density fields are attained with constant pressure/density conditions imposed at the ends. The collision parameter is often tuned during this iterative process to vary the effective viscosity in order to obtain results across a range of Re numbers.
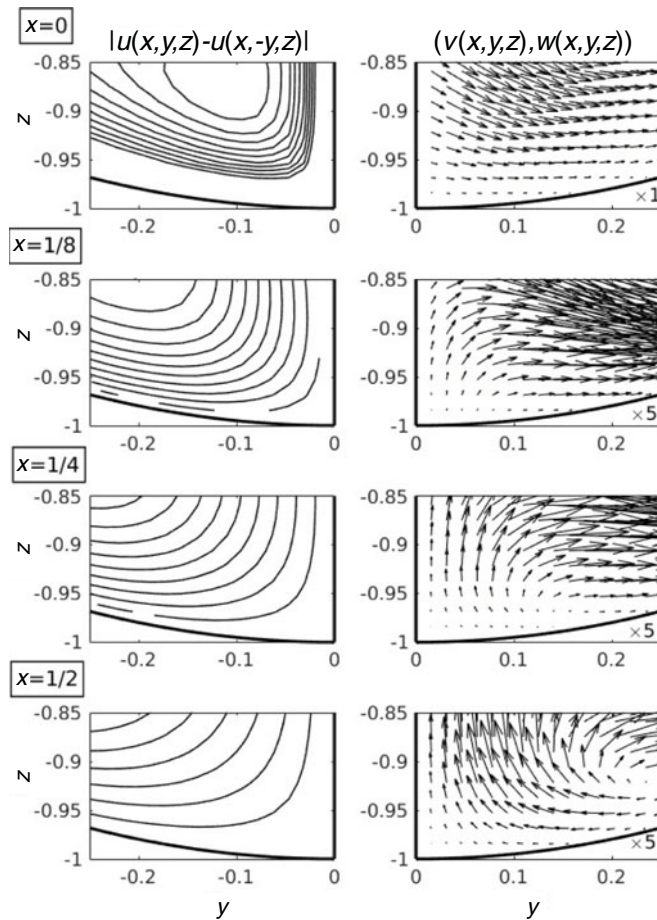
FIGURE 3. Results from 3D lattice-Boltzmann computations of a pressure-driven flow with Re = 245 here. Flow fields are shown at nondimensional axial locations $x = 0$, 1/8, 1/4 and 1/2. The left plot shows a contour plot of the axial velocity difference in the two downstream vessels at the specified axial locations. The ten contours shown represent equally spaced values from 50% to 95% of the maximum velocity difference measured in the downstream vessels. The right plot shows scaled vectors of (v, w) crossflow (the $\times$ 1 or $\times$ 5 shown is the relative scaling) at each axial cross section in one of the downstream vessels.

Some results from the lattice-Boltzmann simulations are presented in Figure 3 with further results appearing later, in Section 5, when comparisons with the predictions of the asymptotic analysis are made. Figure 3 is obtained from a computation of steady flow through the branching geometry shown in Figure 2 that has 601 equally spaced lattice points across its length and 129 lattice points across its diameter. From nondimensionalizing length scales on the cylinder radius, a minimum spacing of $dx, dy, dz = 1/64$ between neighbouring lattice points is obtained. A thin

straight symmetrically bifurcating divider starts halfway along its length, that is, 301 lattice points from the upstream end. The location of the divider is defined in nondimensionalized Cartesian coordinates as occupying $y = 0$, $x > 0$ and $-1 < z < +1$ and a nonsymmetric steady flow is generated by fixing $\sum_i F_i(\mathbf{x}, t) = 1$ at all upstream lattice nodes and $\sum_i F_i(\mathbf{x}, t) = 1 - 0.009$ and $\sum_i F_i(\mathbf{x}, t) = 1 - 0.010$ either side of the divider respectively at all downstream lattice nodes. A collision frequency $\omega = 1.89$ was chosen and the internal streaming and collision process given by (3.1) is repeated until the sum across all internal nodes of the relative error in the axial velocity between each subsequent iteration falls below $5 \times 10^{-8} \times$ (total number of nodes). The Reynolds number is then determined by $3 \times 64 \times \bar{U}_0/(\omega^{-1} - 0.5)$, where $\bar{U}_0$ is the maximum absolute velocity recorded across the upstream end of the cylinder.

The left-hand plots in Figure 3 show the axial velocity difference $|u(x, y, z) - u(x, -y, z)|$ between the two daughter vessels at different cross-sections downstream of the divider (nondimensionalized on vessel radius). This velocity difference is shown as it represents the first-order nonsymmetric perturbed flow field which can be straightforwardly compared to the predictions of the asymptotic analysis that follows. A significantly large perturbed axial flux appears to be present in the corner region just downstream of the divider edge $x = 0$, which is expelled from the corner over a short distance as the flow moves downstream. The right-hand plots show the scaled (v, w) crossflow field that is present in the same corner region, revealing the emergence of a swirling flow initiated in the corner of the divider which creeps quickly around the outer wall away from the divider further downstream.

4. Analysis

The analytical focus is on axial lengths of order unity and relatively small disturbances with Re assumed to be large, with the wall-shear factor $\lambda(s)$ supposed to be of order unity. An effectively inviscid core is expected across the majority of the tube, along with a viscous (or, more correctly, a viscous-inviscid) layer at every wall present. Both end-pressure and wall-shape effects are accommodated in this study. The former effects are found to act mostly at the outer wall of the branching configuration, whereas the shape effects are of two kinds, namely those due to the shape of the inner walls or dividers and those due to the outer wall shaping. Each significantly impacts the behaviour of the wall layer, since it is especially sensitive, but there is a core effect also. So the core and the wall layer are examined next.

4.1. The scales and structure   We take the small characteristic nondimensional pressure magnitude p as given, by virtue of the end-pressure constraints in the tubes; the consequent reasoning establishes the range of appropriate p for large Re. We concentrate on the range

$$|p| \ll \mathrm{Re}^{-2/3}, \tag{4.1}$$

(which corresponds to flow rates satisfying $1 \ll \mathrm{Re} \ll |p|^{-3/2}$). The reason for this is that, in intrinsic coordinates, a wall layer with small n is expected, when Re is large, in which the typical u is λn plus a small disturbance, u_1 say, of magnitude

significantly less than λn. Here, u and λn are equal to the first approximation because of the incoming wall shear λ (observe that the tangent to the vessel wall may not coincide exactly with the x-direction, but is approximately so at the very least). The main inertial, pressure-gradient and viscous forces are then represented in magnitude by nu_1, $|p|$, $u_1/(\text{Re}\,n^2)$, respectively, since x is of $O(1)$. Hence n must be of size $\text{Re}^{-1/3}$ typically, while u_1 is of size $\text{Re}^{1/3}|p|$; this is smaller than the λn term as assumed, provided that Re lies within the range specified by (4.1). Using a numerical example for illustration, if the nondimensional pressure variation $|p|$ is as small as about 0.025 say, then from (4.1) the range of Re under consideration is from around 1 to 240, as a first estimate; this is a range which is certainly of some physical concern as well as of clear modelling interest in terms of flow reversal, for example.

Moving on to wall-shaping effects, the wall-layer scalings above suggest examination of outer-wall shape distortions whose typical thickness is of the order $\text{Re}^{-1}|p|$, to compare directly against the influences of the end-pressures. That, in turn, points to consideration of divider thicknesses of a similar size. The dividers, however, provoke pressures in the core flow that are larger than those in the wall layer, because of the enhanced inertia in the core. Accordingly, if wall shaping is present, different sizes of pressure variation should be anticipated in the core and in the wall layer, even when the shape distortions at the outer wall and at the dividers are comparable. The arguments just used serve to guide the solution expansions presented below, given that the scaled pressure in the mother tube upstream is P_0, and the similarly scaled daughter tube pressures downstream are P_k, $k = 1, \ldots, K$, for K daughters altogether with $(K - 1)$ dividers.

The core motion, being a perturbation of the incoming quasi-unidirectional motion with velocity profile denoted $U_0(y, z)$ and wall-shear $\lambda(s)$ in the mother tube, has the expansion

$$[u, v, w, p] = [U_0(y, z), 0, 0, 0] + \cdots + \varepsilon\text{Re}^{-1/3}[u', v', w', p'](x, y, z, T) + \cdots, \quad (4.2)$$

where the coordinates x, y, z, T are all of $O(1)$ and the scaled velocity and pressure perturbations u', v', w', p' are also of $O(1)$. The first dotted $(\cdots)$ contribution in (4.2) denotes the contribution of the symmetric case [6, 8, 31], which is without divider-thickness or end-pressure effects, whereas the $\varepsilon\text{Re}^{-1/3}$ contribution shown in (4.2) is due to the nonsymmetry now present. The amplitude factor ε is small and must be determined by careful consideration of the different pressure-scales described above, as well as the Blasius-like viscous thickness generated on each divider. Its value is identified later as $\text{Re}^{-1/3}$ by virtue of the typical corner vortex considered in Section 4.4. We take the typical pressure p then to be of $O(\varepsilon\text{Re}^{-2/3})$ in the wall layer, and $O(\varepsilon Re^{-1/3})$ in the core. Thus, by incorporating the corner vortex, the corresponding imposed end pressures are $O(\text{Re}^{-1})$. The time scale t_s, say, is assumed to be large. Hence, the core flow response is quasi-steady, giving the governing equations for the vector $\mathbf{u}' = (u', v', w')$ as

$$\nabla \cdot \mathbf{u}' = 0, \quad\quad\quad (4.3a)$$

$$U_0\mathbf{u}'_x + (v'U_{0y} + w'U_{0z}, 0, 0) = -\nabla p' \quad\quad\quad (4.3b)$$

from the mass conservation and momentum balances. Here ∇ stands for the gradient operator $(\partial_x, \partial_y, \partial_z)$. It follows from (4.3) that

$$\nabla^2 p' = \frac{2(U_{0y} p'_y + U_{0z} p'_z)}{U_0} \tag{4.4a}$$

holds for the pressure perturbation p', subject to the conditions

$$p' \to 0, \quad \text{as } x \to \pm\infty, \tag{4.4b}$$

$$\frac{\partial p'}{\partial n} = -U_0^2 \frac{\partial^2 f_k^+}{\partial x^2} \quad \text{at } y = y_k^+, \tag{4.4c}$$

$$\frac{\partial p'}{\partial n} = -U_0^2 \frac{\partial^2 f_k^-}{\partial x^2} \quad \text{at } y = y_k^-, \tag{4.4d}$$

$$p' \to 0 \quad \text{as } n \to 0 \text{ at the outer wall.} \tag{4.4e}$$

These boundary conditions reflect, respectively, the upstream and downstream end pressures (the zeros seen upstream and downstream in (4.4b) echo the earlier discussion on different pressure magnitudes), the tangential flow conditions on the dividers, and the necessary matching with the wall-layer flow. The f_k values represent the scaled thicknesses of the $(K - 1)$ internal dividers and y_k their locations; these are the main shaping effects within the core. Thus the size of ε allows for the first appearance of shape effects, in (4.4c) and (4.4d), but its relative largeness accounts for the condition (4.4b). Regarding this condition further, the pressure conditions model not only those relevant to simulations as described in Sections 3 and 4.2 but also in principle those relevant to large networks. Conditions (4.4c) and (4.4d) in detail stem from the requirement of tangential flow via the momentum balances, while the wall-layer matching condition (4.4e) is considered in more detail below. Local analysis shows that p' behaves as $\lambda(\partial^2 A/\partial x^2)n^3/3$ as $n \to 0$, where the function $A(x, s, T)$ represents the shaping effects from the core. Defining $v_1 = \varepsilon \text{Re}^{-1/3} v'_1$ and $w_1 = \varepsilon \text{Re}^{-1/3} w'_1$ as the leading order velocity components in the n and s cross-plane directions, respectively, in the approach to the outer wall that leaves $v'_1 \sim n$, $p' \sim n^3$ and $w'_1 \sim n^2$, but with a tangential slip velocity

$$u' \to A(x, s, T) \quad \text{as } n \to 0,$$

in the axial direction.

In the viscous wall layer the implied flow solution is expressed in the form

$$[u, v_1, w_1, p] = [\text{Re}^{-1/3} \lambda N, 0, 0, 0] + \cdots$$
$$+ \varepsilon[\text{Re}^{-1/3} U, \text{Re}^{-2/3} V_1, \text{Re}^{-1/3} W_1, \text{Re}^{-2/3} P] + \cdots, \tag{4.5}$$

where $n = \text{Re}^{-1/3} N$. The outer wall is prescribed by $n = \varepsilon \text{Re}^{-1/3} F(x, z, T)$, giving $N = \varepsilon F(x, z, T)$. The orders of the velocities and pressure in (4.5) are required for conservation of mass and momentum. The time scale specifically has $t = \text{Re}^{1/3} T$ (so t_s is identified with $\text{Re}^{1/3}$) to affect the wall-layer dynamics and is thus relatively slow

as supposed in the earlier argument, whereas x, s are again of order unity. Hence, the unsteady viscous 3D wall-layer equations

$$U_x + V_{1N} + W_{1s} = 0, \tag{4.6a}$$

$$U_T + \lambda N U_x + V_1 \lambda + W_1 \lambda_s N = -P_x + U_{NN}, \tag{4.6b}$$

$$W_{1T} + \lambda N W_{1x} = -P_s + W_{1NN}, \tag{4.6c}$$

apply with the unknown scaled pressure $P(x, s, T)$ being independent of N, because the normal momentum balance requires $\partial P / \partial N$ to be zero at leading order. The boundary conditions on the wall-layer system are

$$U = -\lambda F, \; V_1 = W_1 = 0 \quad \text{at } N = 0, \tag{4.6d}$$

$$U \to A(x, s, T), \; W_1 \to 0 \quad \text{as } N \to \infty, \tag{4.6e}$$

$$(U, V_1, W_1) \to 0, P \to P_0(T) \quad \text{as } x \to -\infty, \tag{4.6f}$$

$$P \to P_k(T) \quad \text{as } x \to +\infty \text{ in the } k\text{th daughter.} \tag{4.6g}$$

The scaled mother pressure $P_0(T)$ and the scaled daughter pressures $P_k(T)$ are those that were introduced earlier on, although now with explicit allowance for their possible unsteadiness. The boundary conditions above reflect the no-slip conditions at the distorted wall in (4.6d), the match to the core flow in (4.6e) (this leads to an algebraic decay in Y), and the upstream and downstream pressure conditions. Shaping effects are present in the contributions A, F, due to the core and the outer wall in turn. To repeat, we have taken the pressure and shape to have comparable effects in the wall layer at this stage. Further, if ε is $O(\text{Re}^{-1/3})$ or less, then an extra contribution $(\mu/2)N^2\text{Re}^{-2/3}$ is needed in the expression for u in (4.5) to account for the incident $O(1)$ velocity profile curvature μ; associated with that an extra term $(-\mu\text{Re}^{-1}x + \text{constant})$ is required in the pressure p. Implicit also throughout all this, is the requirement of

$$\text{periodicity in } s \tag{4.7}$$

for all the velocities and pressures.

    Several points can be made at this stage. First the shape effects as seen in the wall layer are clearly two-fold, coming not only from $A(x, s, T)$, which represents the influence of the divider shaping in the core, but also from $F(x, s, T)$ due directly to the outer wall shape. Again, the slip velocity A acts in the wall layer as a given negative displacement, in view of the contributions to the axial velocity in (4.5) and the condition (4.6e). Shape effects will be examined in detail in Section 4.3. The end-pressure (or pressure-driven) effects are in contrast to the shape effects in the sense that the former, which are to be considered in Section 4.2, are confined to the wall layer to leading order. Such pressure-driven flows have A being zero and so are not influenced directly by any pressure p' in the core. Instead the induced wall pressure in such cases dictates what the core pressure response p' must be, allowing for an amplitude factor reduced from that in the general case. The wall-layer responses also imply the existence of a significant longitudinal vortex in each corner (see Section 4.4). Finally here, the argument also extends to unsteady motions, and likewise allows for nonuniform $\lambda(s)$ as above, as well as other realistic effects.

4.2. Pressure-driven flows The configuration for pressure-driven flows applies for two or more daughters where the flow is driven merely by pressure differences, so that the shape-effect forcings from the core and the outer wall are all absent. Thus F and A in (4.6d) and (4.6e) are both zero here, and steady flow is assumed for now. The wall-layer flow problem set out in the previous section then has an unusual solution that V_1 is identically zero, and hence adding the x-derivative of equation (4.6b) to the s-derivative of (4.6c) yields Laplace's equation

$$\widehat{\nabla}^2 P = 0, \tag{4.8}$$

for the unknown outer-wall pressure $P(x, s)$, where $\widehat{\nabla}^2$ denotes the 2D Laplacian $\partial^2/\partial x^2 + \partial^2/\partial s^2$. The boundary conditions on P are those of the prescribed pressures far upstream and downstream as written in (4.6f) and (4.6g), supplemented by the requirement (4.7) at all finite x stations. The reduction of the originally 3D wall-layer flow problem to the 2D Laplacian problem (4.8) is notable.

Being driven by spatially constant end-pressures acting up- and downstream means that the pressure response in between involves eigensolutions in effect. These can be seen in the following basic case of two daughters, $K = 2$ with end pressures in the two daughters such that $P_2 = -P_1$. In this case there is an exact solution given by a conformal mapping of the form

$$\frac{P}{P_1} = \pm \operatorname{Real}(1 + e^{-2\xi})^{-1/2}, \tag{4.9}$$

where $\xi = x + is$ (with $i = \sqrt{-1}$), and the branching divider terminates upstream at $x = 0$ with the junctions of the outer wall and the divider being symmetrically positioned at $s = \pi/2$ and $s = 3\pi/2$. The solution exhibits the irregular response of the pressure near the leading edge of the divider in the present nonsymmetric setting, a response which is more severe than in the symmetric setting [20]. There is also the series representation of the form

$$\frac{P}{P_1} = \begin{cases} e^x \cos s - \frac{1}{2} e^{3x} \cos 3s + \frac{3}{8} e^{5x} \cos 5s + \cdots & \text{for } x < 0, \\ 1 - \frac{1}{2} e^{-2x} \cos 2s + \frac{3}{8} e^{-4x} \cos 4s + \cdots & \text{for } x > 0, \end{cases} \tag{4.10}$$

which shows the eigenforms clearly. Note that these expansions, in which the nth coefficient is $(-1/2)(-3/2) \cdots (3/2 - n)/(n - 1)!$ for $n > 3$, apply for the daughter with end pressure P_1; the pressure in the other daughter is, of course, equal and opposite. This short-scale wall pressure response is shown in Figure 4.

For $K > 2$, conformal mapping or series solutions can again be applied (we have carried out the former) but, in practice, seem better used as a check to a computation. The second-order computational method adopted involves a line-by-line relaxation in which, essentially, (4.8) is represented by five-point differencing while the boundary conditions required at each divider, at each end station and to ensure periodicity, are treated by means of local expansions. In fact it is more convenient to work in terms of the integral of P with respect to x as the unknown function of x, s. The irregular
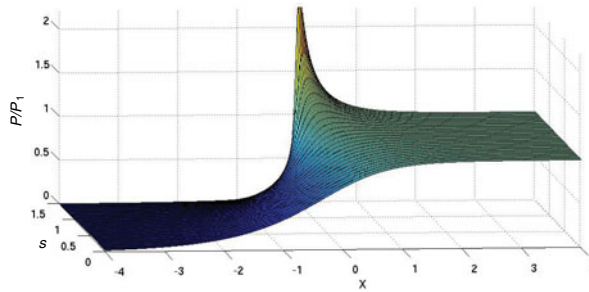
FIGURE 4. The scaled wall pressure, $P(x, s)/P_1$, in the first daughter, as given by the exact solution (4.9) for the pressure-driven case where $K = 2$.

behaviours near the leading edges of the dividers present can then be accommodated accurately through a rotation of the five-point differencing nearby, since the integral function is finite at each leading edge. The methodology is also more easily extendable to more complex cases, see later, as well as maintaining the Cartesian-like description on the wall. The wall pressure solutions P are shown in Figure 5 for a $K = 4$ case and a $K = 8$ case. For the $K = 4$ case, the imposed end-pressures in the downstream vessels are $(4, 0, 0, -4)$, whereas for the $K = 8$ case the imposed downstream end pressures are $(7, -1, -1, -1, -1, -1, -1, -1)$. The figures also present some of the corresponding induced scaled wall-shear distributions obtained analytically from (4.6a)–(4.6c), with $\lambda(s)$ constant to represent a symmetric incident mother flow, T-dependence being absent and with P found as just above. For instance, the integral form [31, 32]

$$\tau_1 = \Phi \int_{-\infty}^{x} (x - \xi)^{-2/3} \frac{\partial}{\partial \xi} P(\xi, s) \, d\xi, \qquad (4.11)$$

with $\lambda^{1/3}\Phi = -3^{1/6}(\Gamma(2/3))^2/2\pi = -0.35047 \cdots$ determines the axial shear stress perturbation τ_1, and a similar integral yields the cross-plane shear stress τ_2, where $\tau_1 = \partial U/\partial N$ and $\tau_2 = \partial W_1/\partial N$ at the wall ($N = 0$), respectively (see also Appendix A).

The main effects present in the wall-layer results are those of different effective suctions into the daughter tubes as they compete with each other to draw fluid from the mother tube. In every case, a sufficiently low end-pressure downstream in a daughter tends to draw fluid into that daughter, causing an increase in the corresponding axial shear stress and directions of the neighbouring cross-plane shear stresses that indicate cross-plane movement of fluid towards the lower-pressure daughter. The maximal effects in the wall-shear stresses occur quite close to the daughter entrances. Upstream of the entrances the wall-shear-stress response is essentially exponential in form, whereas downstream of the entrances the response involves a comparatively slow algebraic ($x^{-1/3}$) decay, consistent with (4.11). The dominant response sufficiently far upstream is seen to be an axially symmetric one, by the way. Extremes can also
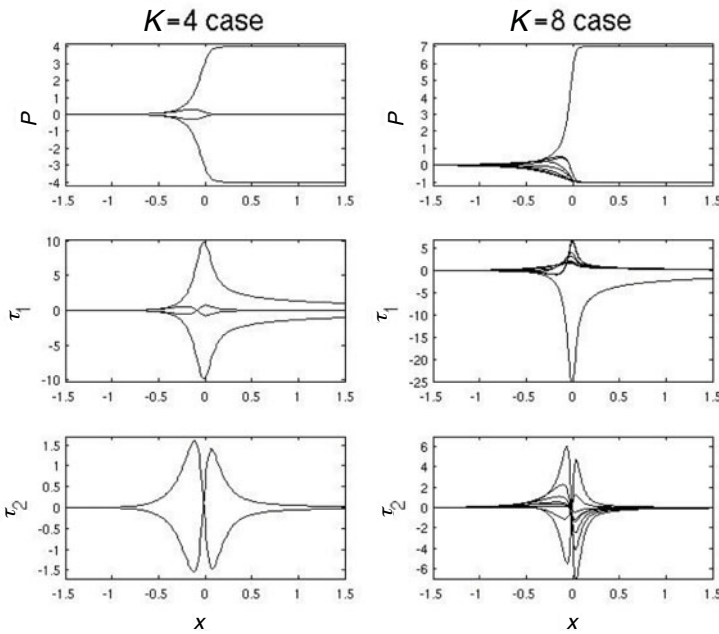
FIGURE 5. Scaled wall pressure and shear stresses obtained in two pressure-driven cases with $K = 4$ and $K = 8$, respectively. Here, curves of the different solutions correspond to the fixed s values associated with the centreline on the outer wall of each daughter vessel.

be investigated such as for large values of K [33], where the wall pressure problem becomes approximately one holding for $x < 0$ alone, and for small daughter-widths which lead to a global sink influence accompanied by a local region close to the entrance of the daughter tube.

The flow configuration so far has the sum of the end pressures being equal to zero. If the sum is nonzero, then consideration can be given to adding in a further degree of nonlinearity in the flow response as compensation. Varying gap-widths may also be incorporated as suggested earlier. More significantly, it is possible to move on to find the core solution forced by the known wall pressures determined as above and hence predict the swirl provoked in the core due to the pressure-driven configuration. Here the amplitude of the velocity and pressure perturbations is of typical size $\varepsilon \mathrm{Re}^{-2/3}$ from (4.5), rather than the size $\varepsilon \mathrm{Re}^{-1/3}$ in (4.2). Thus, the newly scaled pressure in the core p is obtained from (4.4a)–(4.4e), but subject to generally nonzero downstream end pressures instead of (4.4b), zero normal pressure gradient conditions with $f_k = 0$ replacing (4.4c) and (4.4d) at the dividers, while (4.4e) is replaced by

$$p \to P(x, s) \quad \text{as } n \to 0 \text{ at the outer wall.} \qquad (4.12)$$

Given (4.12), the tangential components in the velocity perturbations grow like $1/n$ as the outer wall is approached [31, 32]. The corresponding core solutions can be derived from an analysis similar to that in the next subsection.
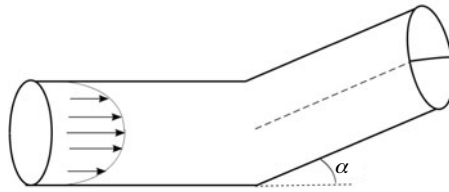
FIGURE 6. Schematic of the antisymmetric case.

4.3. Shape-driven flows In this subsection, we study shape effects where the divider thicknesses f_k for $k = 1, \ldots, (K - 1)$ are no longer zero. Specifically, we look at a single bifurcation, from a mother tube of circular cross-section to straight but divergent daughter tubes, as examined previously in Smith and Tadjfar [37] and extend their original short-scale analysis of the core flow to nonsymmetric bifurcations [37, Appendix A]. Bifurcation angles here are assumed to lie between the two critical values identified in [37], $\mathrm{Re}^{-1/3}/\ln \mathrm{Re}$ and $\mathrm{Re}^{-1/2}$, so that the viscous boundary layer is negligible. Smith and Tadjfar originally solved the governing equations of the core (4.4) for a symmetric bifurcation with a symmetry condition on the line $y = 0$ (in cylindrical coordinates here $\theta = s = 0, \pi$) upstream of the divider $x < 0$. This is, in cylindrical coordinates (x, r, θ), also with the velocity profile far upstream $U_0 = \bar{u}(r)$ depending only on the radial coordinate r. Treating the wall shaping as $f(x) = xH(x)$ where $H(x)$ is the Heaviside function and, for convenience, working with the integrated pressure perturbation

$$q = \int_{-\infty}^{x} \tilde{p}(\hat{x}, r, \theta) \, d\hat{x}$$

where $\tilde{p} = p'/\alpha$, a solution was determined of the form

$$q = \hat{q}(r, \theta) H(x) \mp \sum_{n=0}^{\infty} \cos(2n\theta) \sum_{m=1}^{\infty} C_{nm} e^{\mp \gamma_{nm} x} q_{nm}(r), \qquad (4.13)$$

where the eigenfunctions $q_{nm}(r)$ and respective eigenvalues γ_{nm} satisfy a homogeneous ordinary differential equation (ODE) in r and describe the upstream and local downstream influence. On the other hand, $\hat{q}(r, \theta)$ is the remnant component of q that persists far downstream in the daughter vessel with its eigenfunctions determined by an inhomogeneous ODE and conditions of finiteness at $r = 0$ and $\hat{q}(1) = 0$.

To extend this analysis to nonsymmetric divergent bifurcations, the purely antisymmetric case shown in Figure 6 must be examined. The governing equation for q, as defined above, is given by

$$\nabla^2 q = \frac{2}{\bar{u}(r)} \frac{d\bar{u}}{dr} \frac{\partial q}{\partial r} \qquad (4.14)$$

TABLE 1. Symmetric and antisymmetric eigenvalues.

	Symmetric γ_{nm}					Antisymmetric $\tilde{\gamma}_{nm}$			
	$m = 1$	$m = 2$	$m = 3$	$m = 4$		$m = 1$	$m = 2$	$m = 3$	$m = 4$
$n = 0$	3.83	7.02	10.17	13.32	$n = 0$	5.34	8.54	11.71	14.87
$n = 1$	6.73	9.98	13.18	16.35	$n = 1$	8.06	11.36	14.59	17.79
$n = 2$	9.34	12.70	15.98	19.20	$n = 2$	10.59	14.02	17.33	20.58
$n = 3$	11.82	15.30	18.66	21.94	$n = 3$	13.02	16.57	19.96	23.28

in cylindrical coordinates (x, r, θ) where the following boundary conditions are imposed [37]:

$$q \to 0 \quad \text{as } x \to -\infty,$$
$$q \to 0 \quad \text{as } r \to 1-,$$
$$q_y = -\bar{u}^2 \quad \text{for } x > 0 \text{ at } y = 0+.$$

However, unlike Tadjfar and Smith [37], here we impose upstream of the divider the antisymmetric condition

$$q = 0 \quad \text{instead of } q_y = 0 \text{ for } x < 0 \text{ at } y = 0+.$$

A solution of the form (4.13) is sought in each downstream daughter vessel. In the upstream vessel though we assume that the following antisymmetric form holds:

$$q(x < 0) = \sum_{n=0}^{\infty} \sin[(2n + 1)\theta] \sum_{m=1}^{\infty} \mathcal{D}_{nm} \, e^{+\tilde{\gamma}_{nm}x} \, \tilde{q}_{nm}(r).$$

The antisymmetric eigenfunctions $\tilde{q}_{nm}$ and eigenvalues $\tilde{\gamma}_{nm}$ satisfy an ODE similar to that for the symmetric case, but with $4n^2$ replaced by $(2n + 1)^2$; thus $\tilde{q}_{nm}$ solves

$$\frac{d^2\tilde{q}_{nm}}{dr^2} + \left(\frac{1}{r} - \frac{2}{\bar{u}}\frac{d\bar{u}}{dr}\right)\frac{d\tilde{q}_{nm}}{dr} + \left(\tilde{\gamma}_{nm}^2 - \frac{(2n + 1)^2}{r^2}\right)\tilde{q}_{nm} = 0,$$

with boundary conditions $\tilde{q}_{nm}(1) = 0$ and $\tilde{q}_{nm}$ finite at $r = 0$. The regular behaviour near zero can be analysed to show that $\tilde{q}_{nm}(r) \sim r^{2n+1}$ as $r \to 0$ compared to the symmetric case where $q_{nm}(r) \sim r^{2n}$. To calculate the eigenfunctions, we normalize so that $r^{-(2n+1)}\tilde{q}_{nm} \to 1$ as $r \to 0$. Table 1 compares the first few eigenvalues obtained numerically for both symmetric and antisymmetric eigenfunctions, for the case where $\bar{u}(r) = (1 - r^2)$. Importantly, it shows that nonsymmetry in the branching shape *does not* lead to larger-scale upstream influence compared to a perfectly symmetric branching.

Using a combination of symmetric and antisymmetric eigenmodes in the vessels enables us to construct solutions of the core flow for *any* nonsymmetric branching structure of two straight semicircular daughter vessels diverging at different angles

from the axis of the mother tube. In such a case we solve the governing equation for the integrated pressure (4.14) with boundary conditions

$$q_y = \begin{cases} -\bar{u}^2 \tan(\alpha_1)H(x) & \text{at } y = 0+, \\ -\bar{u}^2 \tan(\alpha_2)H(x) & \text{at } y = 0-, \end{cases}$$

where α_1 and α_2 are the divergent angles of the upper and lower daughter respectively (with symmetric branching implying $\alpha_2 = -\alpha_1$), both of which are assumed to lie below the second critical value as described by Tadjfar and Smith [37]; the usual boundary conditions, $q \to 0$ as $x \to -\infty$ and $r \to 1-$, also apply. The general solution in the upstream mother tube thus includes both symmetric and antisymmetric parts, and takes the form

$$q_M = \sum_{n=0}^{\infty} \cos(2n\theta) \sum_{m=1}^{\infty} C_{nm}^M e^{+\gamma_{nm}x} q_{nm}(r)$$

$$+ \sum_{k=0}^{\infty} \sin((2k+1)\theta) \sum_{m=1}^{\infty} \mathcal{D}_{km}^M e^{+\tilde{\gamma}_{km}x} \tilde{q}_{km}(r).$$

The solution in each daughter, $I = 1$ or 2, can be expressed as the sum of exponentially decaying $\cos(2n\theta)$ eigenmodes and a remnant solution that persists downstream; thus

$$q_I = \left(\sum_{n=0}^{\infty} \cos(2n\theta) f_n^I(r) - r \sin\theta \bar{u}^2 \alpha_I \right) H(x)$$

$$- \sum_{n=0}^{\infty} \cos(2n\theta) \sum_{m=1}^{\infty} C_{nm}^I e^{-\gamma_{nm}x} q_{nm}(r),$$

where $\tan(\alpha_I) \approx \alpha_I$ has been assumed. The remnant in this case is the solution to the following forced equation:

$$\frac{d^2 f_n^I}{dr^2} + \left(\frac{1}{r} - \frac{2}{\bar{u}}\frac{d\bar{u}}{dr} \right)\frac{df_n^I}{dr} - \frac{4n^2}{r^2} f_n^I = \begin{cases} \alpha_I \dfrac{4}{\pi}\left(2\bar{u}\dfrac{d\bar{u}}{dr} - r\left(\dfrac{d\bar{u}}{dr}\right)^2 + r\bar{u}\dfrac{d^2\bar{u}}{dr^2} \right) & n = 0, \\ -\dfrac{8\alpha_I}{\pi(4n^2-1)}\left(2\bar{u}\dfrac{d\bar{u}}{dr} - r\left(\dfrac{d\bar{u}}{dr}\right)^2 + r\bar{u}\dfrac{d^2\bar{u}}{dr^2} \right) & n \neq 0, \end{cases}$$

where note that equation (A11) of [37] has now been corrected. For more complex branching shapes, where the daughter vessels are not straight, other forced terms need to be added to the series: for example, shapes defined by exponential dependence require exponential terms.

By means of a simple example, take the case of a side-branching where $\alpha_1 = \alpha > 0$, and $\alpha_2 = 0$. In this case, we note that there is no remnant solution in the second daughter vessel. By expressing

$$\sin((2m+1)\theta) = \pm \sum_{k=0}^{\infty} \beta_{km} \cos(2k\theta) \quad \text{where } \beta_{nk} = \begin{cases} \dfrac{8m+4}{\pi((2m+1)^2-4k^2)} & k > 0, \\ \dfrac{2}{\pi(2m+1)} & k = 0, \end{cases}$$
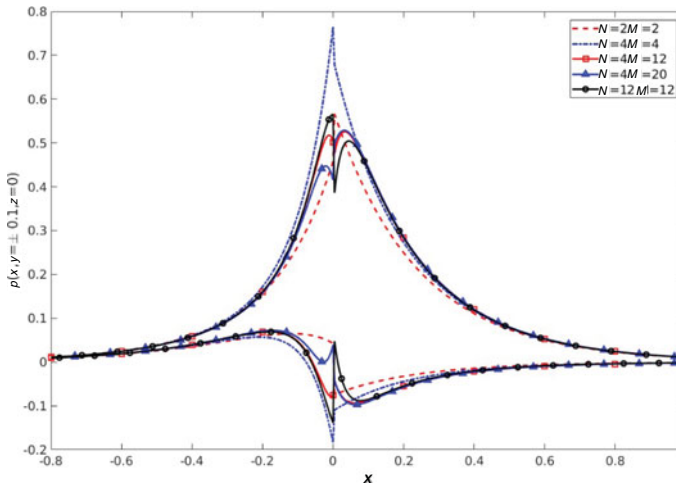
FIGURE 7. Shape effects – side-branching case with $\alpha_1 > 0$ and $\alpha_2 = 0$. Pressure plots on the symmetry plane just either side of the divider plane for various values of N and M (colour available online).

and using the orthogonality of the q_{nm} functions it is possible, by enforcing q and q_x continuous at $x = 0$, to determine all the unknown coefficients by first solving numerically the following matrix equation for a truncated finite set of $\mathcal{D}_{nm}^{\mathcal{M}}$ (for some $0 < n < N$ and $1 < m < M$):

$$\sum_{s=0}^{N}\sum_{t=1}^{M}\beta_{ns}\left(1 + \frac{\tilde{\gamma}_{st}}{\gamma_{np}}\right)\mathcal{D}_{st}^{\mathcal{M}}\int_0^1 \tilde{q}_{st}(r)q_{np}(r)\frac{r}{\bar{u}^2}\,dr = \frac{1}{2}\int_0^1 (f_n^1(r) - r\beta_{n0}\bar{u}^2\alpha)\frac{rq_{np}(r)}{\bar{u}^2}\,dr.$$

The symmetric contribution can then be determined by eliminating the antisymmetric $\sin((2n + 1)\theta)$ term, leading to

$$C_{np}^{\mathcal{M}} = \frac{1}{4\int_0^1 [q_{np}(r)]^2(r/\bar{u}^2)\,dr}\left\{\int_0^1 (f_n^1(r) - r\beta_{n0}\bar{u}^2\alpha)\frac{rq_{np}(r)}{\bar{u}^2}\,dr\right\}.$$

Lastly, the daughter coefficients can be subsequently resolved by substituting the $C_{np}^{\mathcal{M}}$ and $D_{nm}^{\mathcal{M}}$ values back into the continuity conditions for q and q_x at $x = 0$.

Figure 7 shows pressure plots for the side-branching case, obtained for various choices of N and M, on the symmetry plane just either side of the divider plane at $(y, z) = (\pm 0.1, 0.0)$. Although the pressure peaks for $|x| < 0.1$ are not fully resolved, even for small M and N the main features of the upstream and downstream influence generated by the side-branching are broadly well-defined. Furthermore, the trend of the peak values obtained as N and M increase allows a reasonably good estimate of the actual size of the peaks in the upper and lower daughters at $x = 0$ for large N, M. The plot also clearly emphasizes how the most significant upstream influence stems from the symmetric $C_{nm}^{\mathcal{M}}$ contributions in the mother vessel as $x \to -\infty$ (as predicted

by the eigenvalues obtained) leading to an adverse pressure gradient upstream on approach to the lower daughter. This pressure gradient, however, is dramatically reversed to a favourable one, just ahead of entrance to the lower daughter vessel as the antisymmetric $\mathcal{D}_{nm}^{\mathcal{M}}$ components come into play over a shorter distance.

4.4. Corner vortices

The lattice-Boltzmann results shown in Figure 3 indicate significant nonsymmetric flows in the corner region just downstream of the divider edge. The corner vortex for the pressure-driven flow is forced by the behaviour of the wall layer in equations (4.6a) to (4.11), which includes the jet-like behaviour of U and W_1. Given (4.6a) to (4.6g) in the pressure-driven case and $\lambda = 1$ here, the wall layer produces the result $U^* = (i\sigma)^{1/3}P^*L(\eta)$ via the Fourier transform $U^* = \int_{-\infty}^{+\infty} U\,e^{-i\sigma x}\,dx$, where the asterisk denotes the transformed variable and $L(\eta)$ is related [32] to the Airy function $\mathrm{Ai}(\eta)$ via

$$L(\eta) = \mathrm{Ai}(\eta) \int_0^\eta \mathrm{Ai}^{-2}(\eta_2) \int_\infty^{\eta_2} \mathrm{Ai}(\eta_1)\,d\eta_1\,d\eta_2.$$

Hence, there is a transformed axial mass-flux effect given by the finite part of the integral of U^* over all positive N which yields $C_1 P^*$. Here $\eta = (i\sigma)^{1/3}N$ and the constant $C_1 = -0.136\cdots$, approximately; see also Appendix A. A second integration, over θ from 0 to $\pi/2$ and with a sign change, predicts the effective azimuthal flux approaching the corner as, therefore,

$$-C_1 \int_0^{\pi/2} P(x,\theta)\,d\theta. \tag{4.15}$$

The integral here is nonzero at all positive x values because of the form of the pressure in (4.10); the nonzero flux and the associated nonzero swirl velocity $W = W_3(N)$ at $\theta = 0+$ both feed into the corner vortex. The corner vortex is also forced by the spillover of fluid from the other nearby corner region in a sense, but this is merely a mirror effect. The value of the integral in (4.15) at $x = 0+$, in particular, is found to be 1.6 approximately.

The corner region is of small square cross-section having $(1 - r, \theta) = \mathrm{Re}^{-1/3}(Y, Z)$, but $x = O(1)$. The flow solution expands as

$$[u, v, w] = [\mathrm{Re}^{-1/3}\bar{U}_1, \mathrm{Re}^{-2/3}\bar{V}_1, \mathrm{Re}^{-2/3}\bar{W}_1] + \cdots,$$
$$\text{and} \quad p = \mathrm{Re}^{-1}(-g_1 x + d_1 + \bar{P}_1(x)) + \mathrm{Re}^{-4/3}\bar{P}_2 + \cdots, \tag{4.16}$$

where g_1 and d_1 are given constants from the original pipe flow and $\bar{P}_1(x)$ is the value of P on approach to the presently studied corner. Here the unknowns $\bar{U}_1, \bar{V}_1, \bar{W}_1, \bar{P}_2$ depend on x, Y and Z. The scales in (4.16) are implied mostly by the balances between uu_x and $\mathrm{Re}^{-1}u_{yy}, \mathrm{Re}^{-1}u_{zz}$ in the x-momentum equation, with $y \sim z$, and similar balances in the y- and z-momentum equations, allied with the nontrivial continuity equation. Extra terms arise from the surrounding or incident flow properties. The nature of the corner region dictates that $\varepsilon = \mathrm{Re}^{-1/3}$ such that the pressure has the form in (4.16),

owing to the nonlinear balances governing the corner flow. These are

$$\frac{\partial \bar{U}_1}{\partial x} + \frac{\partial \bar{V}_1}{\partial Y} + \frac{\partial \bar{W}_1}{\partial Z} = 0,$$

$$\bar{U}_1 \frac{\partial \bar{U}_1}{\partial x} + \bar{V}_1 \frac{\partial \bar{U}_1}{\partial Y} + \bar{W}_1 \frac{\partial \bar{U}_1}{\partial Z} = \left(\frac{\partial^2}{\partial Y^2} + \frac{\partial^2}{\partial Z^2} \right) \bar{U}_1,$$

$$\bar{U}_1 \frac{\partial \bar{V}_1}{\partial x} + \bar{V}_1 \frac{\partial \bar{V}_1}{\partial Y} + \bar{W}_1 \frac{\partial \bar{V}_1}{\partial Z} = -\frac{\partial \bar{P}_2}{\partial Y} + \left(\frac{\partial^2}{\partial Y^2} + \frac{\partial^2}{\partial Z^2} \right) \bar{V}_1,$$

$$\bar{U}_1 \frac{\partial \bar{W}_1}{\partial x} + \bar{V}_1 \frac{\partial \bar{W}_1}{\partial Y} + \bar{W}_1 \frac{\partial \bar{W}_1}{\partial Z} = -\frac{\partial \bar{P}_2}{\partial Z} + \left(\frac{\partial^2}{\partial Y^2} + \frac{\partial^2}{\partial Z^2} \right) \bar{W}_1.$$

That is, we have a nonlinear vortex motion [6, 8, 10, 31, 37] in the corner. Note that Blyth and Mestel [8] also identified a vortex in the symmetric case where the influence is mild whereas, in the present nonsymmetric setting, the influence is pronounced since the axial mass flux in the corner vortex is comparable with that in the core and the wall layer. The boundary conditions on the vortex include no slip at the walls $Y = 0$, $Z = 0$, matching with the Blasius-like layer on the divider [6, 8, 31], and crucially the matching condition

$$\bar{W}_1(Y, Z) \to W_3(Y) \quad \text{as } Z \to \infty$$

to take account of the swirl from the wall layer above, accompanied with a starting condition at $x = 0+$. The main point perhaps is that the nonlinear mechanism here means that flow separation can occur, despite the relatively small responses in the core and wall layers. Higher imposed end pressures would lead to restructuring arising first in the corner vortex. Numerical treatment is necessary in general, possibly as implemented by Bowles et al. [9, 10].

5. Comparing analysis and computations

Steady flow solutions were obtained computationally as described in Section 3, through iterating the internal streaming equation (3.1) with no-slip conditions and long-range unequal pressure drops imposed, and the viscosity was tuned via the collision parameter ω to obtain steady flow solutions across a range of Re values. To validate the short-scale effects predicted by the asymptotic analysis of pressure-driven flows in Section 4.2, we need to separate the short-scale pressure jump (as shown in Figure 4) from the longer-scale nonsymmetric pressure gradients driving the upstream flow. The schematic of the computational domain in Figure 2 highlights how this was done to enable the mass-flux perturbation obtained from the lattice-Boltzmann simulations to be directly compared to the pressure-driven asymptotic theory. Once converged steady flow and pressure fields were obtained, the short-scale pressure jump $\pm P_1$ was calculated from the wall pressure difference ΔP across the symmetry line at the axial position $x = 0$, where the divider starts, via the relation $|\Delta P| = \sqrt{2}P_1$, obtained from equation (4.9) of the wall-layer analysis. The mass-flux perturbation, calculated as half of the difference between the axial mass fluxes obtained in the downstream
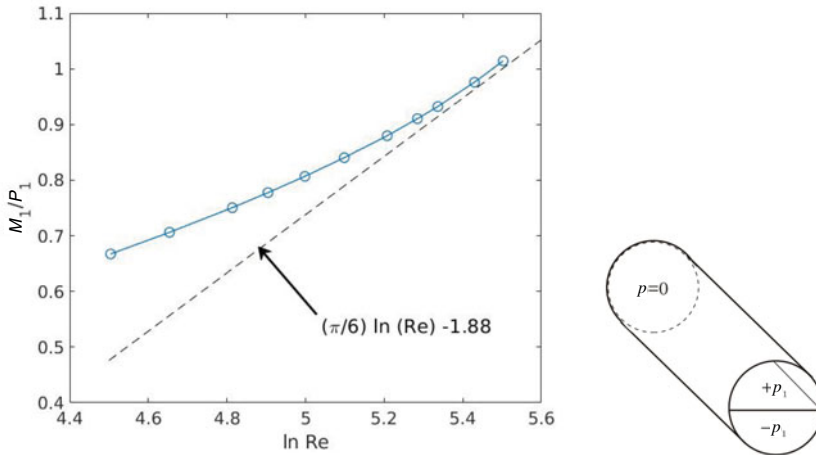
FIGURE 8. Mass-flux comparison between lattice-Boltzmann simulations and the asymptotic analysis for a one-to-two branching. Circles are LBM simulations in a lattice containing $601 \times 129 \times 129$ points. The straight dashed line is the asymptote obtained from the pressure-driven analysis.

vessels with end pressures of opposite sign, and given in the $K = 2$ case as

$$M_1 = \frac{1}{2} \left| \int_{-\pi/2}^{\pi/2} \int_0^1 u(x, r, \theta) r \, dr \, d\theta - \int_{\pi/2}^{3\pi/2} \int_0^1 u(x, r, \theta) r \, dr \, d\theta \right|$$

was determined at various axial locations downstream of the divider start. Figure 8 shows a plot of M_1/P_1 against $\ln \text{Re}$ for the $K = 2$ case, adopting the geometry described in Section 3.

For the pressure-driven case, one reasonable validation between the analysis and the lattice-Boltzmann computation is to examine the mass-flux perturbation in one daughter vessel of cross-section $\mathcal{D}$. Given the expansion (4.5) and the algebraic decay of the jet-like U profile in the outer reaches of the wall layer, the analysis produces logarithmic predictions of

$$\frac{\pi}{3K} \ln \text{Re} + O(1) \tag{5.1}$$

for the axial mass-flux effect in each daughter; this asymptote is displayed as a dashed line in Figure 8. The constant term in the asymptote arises from mass-flux contributions from the core flow, including

$$\int_0^1 \int_{-\pi/2}^{+\pi/2} \frac{1}{U_0^2(r)} \frac{dU_0}{dr} \int_{-\infty}^{\infty} \frac{\partial q}{\partial r}(\hat{x}, r, \theta) \, r \, d\hat{x} \, dr \, d\theta,$$

as well as those contributions arising in the corners, obtained from (4.15), and the finite-part contribution from the outer-wall layer (see Appendix A). The agreement seen here between the results of simulation and analysis is increasingly affirmative as Re increases. Similar agreement between computations and analysis was found in

the $K = 4$ pressure-driven case computed in a similar cylindrical geometry with four identically shaped downstream vessels of quadrantal cross-section.

6. Nonuniform incident wall-shear

When the incident pipe flow itself is nonuniform such that its wall shear varies with s, then 3D nonsymmetry holds again. In general, the incident motion in the mother tube should be expected to be complex, for example 3D, and/or not fully developed. This background nonuniformity affects significantly the local pressure-driven motion. The wall pressure equation is now found from (4.6a)–(4.7) to become

$$\nabla_2^2 P - \frac{3}{2\lambda(s)} \frac{d\lambda}{ds} \frac{\partial P}{\partial s} = 0. \tag{6.1}$$

This was solved computationally for various $\lambda(s)$ distributions. The scaled wall-shear stresses then follow from the previous algebraic manipulation giving

$$\Phi^{-1}\tau_2 = \mathcal{I}(P_s) = \int_{-\infty}^{x} \frac{P_s(\xi, s)}{(x - \xi)^{2/3}} \, d\xi, \quad \frac{\partial \tau_1}{\partial x} = -\frac{\partial \tau_2}{\partial s} + \frac{1}{2\lambda(s)} \frac{d\lambda}{ds} \tau_2. \tag{6.2}$$

Upon integration, this yields the following equation for the axial shear:

$$\tau_1 = -\frac{2}{3\lambda(\theta)} \frac{d\lambda}{ds} \int_{-\infty}^{x} \tau_2(\zeta, s) \, d\zeta + \Phi \mathcal{I}(P_x). \tag{6.3}$$

Results are presented in Figure 9 for a nonuniform incident shear of the form $\lambda(s) = 1 + 0.8 \sin(s)$.

Extremes of interest are for the scaled incident shear $\lambda(s)$ becoming small or large locally near some particular s value, say s_0. The scalings then act as follows. If λ is small and positive then an equal scaling of $(s - s_0)$ and x retains all the contributions in the governing equation (6.1) and so the full system applies, the only change being that the streamwise and spanwise ranges become infinite in effect. The local problem for pressure thus appears to be a closed one. Over the main length scale of $O(1)$ values of x, however, the streamwise derivatives in (6.1) generally have negligible effect and thus the scaled pressure is simply $\Pi_0(x)$, the local pressure variation. Globally in that case, the governing equation (6.1) also continues to hold but now λ behaves as say $\lambda_2(s - s_0)^2$ near $s \approx s_0$ where λ_2 is a positive constant. For x of order unity the pressure P then responds as $\Pi_0(x) + O((s - s_0)^2)$ near $s \approx s_0$; here $\Pi_0(x)$ is determined by the global problem. Similar working applies wherever λ is large and positive locally.

7. Unsteady flows

We consider the pressure-driven setting with the end pressures being dependent on the scaled time T, again for values of K of 2 or more. The quasi-planar equation (4.8) still controls P here when $\lambda(s)$ is uniform, with V_1 being zero and the 3D momentum effects cancelling each other out. So the pressure solutions of Section 4.2 continue to apply in a quasi-steady fashion.
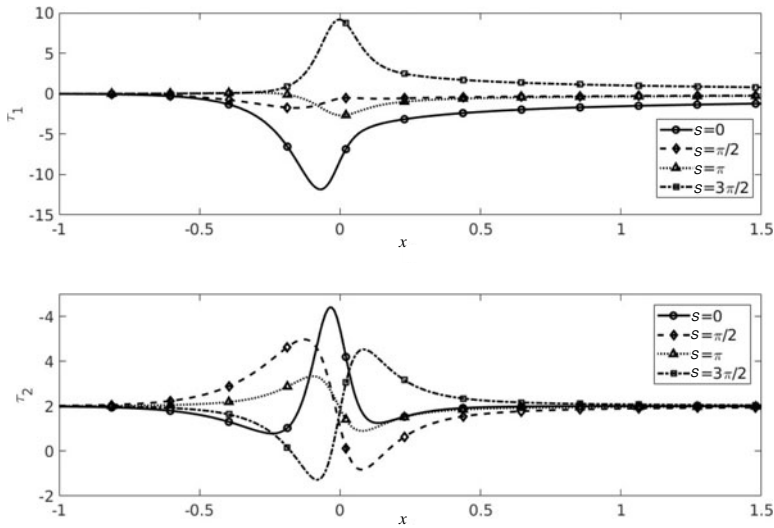
FIGURE 9. Scaled wall-shear stresses obtained from integrals (6.2) and (6.3) in the case of a nonuniform incident wall-shear. In this one-into-four branching case, $\lambda(s) = 1 + 0.8 \sin(s)$ and the numerical simulations calculate the wall pressure in the nondimensional range $-3 < x < 3$ and $0 < s < 2\pi$.

The velocity fields in contrast remain truly unsteady through (4.6a) to (4.6g), and that feature affects the scaled wall-shears. Here, we solve the system (4.6a) to (4.6c) driven by the new given $P(x, s, T)$ forms. Supposing $\lambda(s)$ is uniform so that V_1 is identically zero, then the axial momentum equation

$$\frac{\partial U}{\partial T} + \lambda N \frac{\partial U}{\partial x} = -\frac{\partial P}{\partial x} + \frac{\partial^2 U}{\partial N^2}$$

has to be solved to determine U and hence τ_1, while W_1 and hence τ_2 can simply be obtained afterwards from the continuity balance

$$\frac{\partial U}{\partial x} + \frac{\partial W_1}{\partial s} = 0$$

from (4.6a) with $V_1 = 0$.

In cases of fixed-frequency behaviour proportional to $e^{-i\Omega T}$, for example, the Fourier transform in x ($x \to \sigma$) can again be applied to give the scaled wall-shear solution

$$\tau_1^* = -\text{Real} \left\{ (i\sigma)^{2/3} P^* \frac{1}{\text{Ai}(\eta_0)} \int_{\eta_0}^{\infty} \text{Ai}(\eta) \, d\eta \right\},$$

where $\eta_0 = -\Omega(i\sigma)^{2/3}/\sigma$ is complex and the factors of $e^{-i\Omega T}$ are assumed. The same approach of using the transform holds in principle for arbitrary forcing, but in practice it is more fruitful to apply the methodology of Section 4.2 to determine the velocity profiles for instance.
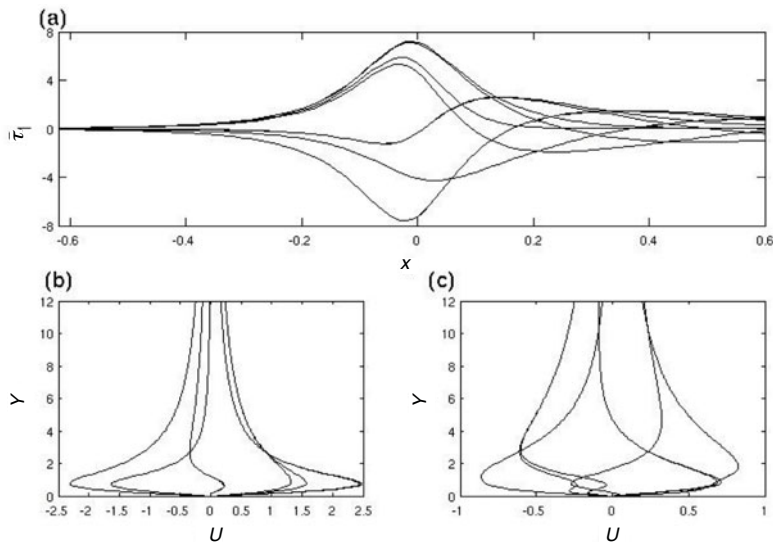
FIGURE 10. Unsteady flow: periodic fixed-frequency forcing starting from rest in the form sin(t) for the case $K = 4$. (a) Evolution of the scaled axial wall-shear stress τ_1 versus axial location over two periods of oscillation. (b) Corresponding velocity profiles at $x = 0$ against Y over two periods of oscillation. (c) Corresponding velocity profiles at $x = 0$ against Y but for a higher frequency forcing, sin($4t$), over eight periods of oscillation.

Results for two representative flows are given in Figures 10(a–c) and 11(a,b). Both cases have all the end pressures being proportional to a function of time; the pressure profiles are as in Figure 5. First, in Figure 10(a–c), a fixed-frequency forcing is started from rest: Figure 10(a) gives the evolution of the wall-shear stress τ_1 versus x over 10 equally spaced time intervals; the corresponding velocity profiles at zero x are in Figure 10(b); Figure 10(c) shows the responses at four times the frequency of the original. It is observed that where x is of order unity, in the middle portion of the combined motion through the mother and daughters, a temporally periodic state is set up relatively quickly, within two time periods effectively except near the wall at higher frequency. Further downstream, however, a decaying wave is seen to travel with the flow. In the second case shown in Figure 11(a,b) the downstream end pressures are instead ramped up and then maintained at uniform levels: (a) shows τ_1 while (b) displays the zero-x velocity profiles. This case yields an apparently quite rapid approach to the steady state in the middle portion of the flow, but slow evolution further downstream. Analytical properties are obtainable for small times T and for extreme time-scales such as at high or low frequencies.

8. Conclusions

Four substantial points should be highlighted in conclusion here. First, as far as we know, this combined numerical (lattice-Boltzmann) and analytical (asymptotic) study
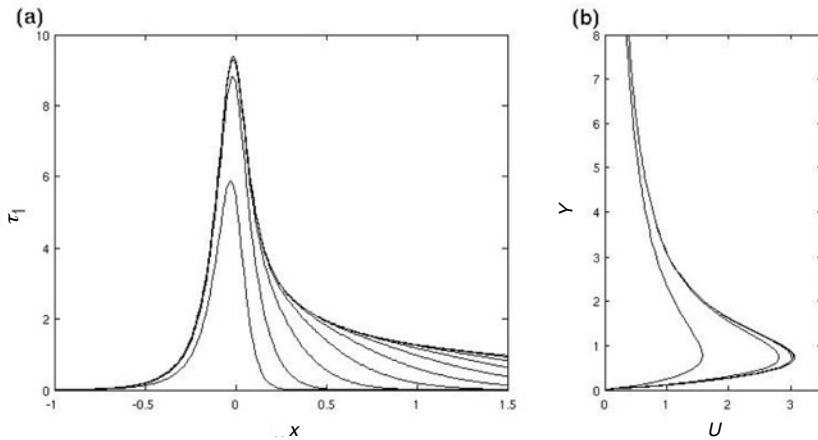
FIGURE 11. Unsteady flow: same as in Figure 10 with low frequency but forcing is fixed once $t = \pi/2$ (ramp-up forcing). (a) Evolution of the scaled axial wall-shear stress τ_1 versus axial location for $t = 0.2, 0.4, \ldots, 2.0$. (b) Corresponding velocity profiles at $x = 0$ against Y.

is the first such theoretical work to tackle, in detail, the 3D nonsymmetric flow through a branching pipe, and to shed light on several novel features of interest emerging in these flows. The branching involved is from a single mother vessel to two or more daughter vessels and the incident motion in the mother pipe has an arbitrary form of velocity profile subject to no slip at the vessel walls. Secondly, the study has identified a universal prediction for the difference in mass flux that arises when unequal pressure differences are imposed in the branching system, at increased Reynolds numbers. The nondimensional mass-flux difference produced is proportional to the logarithm of the Reynolds number multiplied by a scaled pressure difference, with the coefficient of proportionality as given in equation (5.1). This formula agrees fairly well with the direct numerical trends as the Reynolds number (based on the typical cross-sectional length) increases beyond about 100 in the current settings. The above universal formula is for the pressure-driven case, while a form for the corresponding shape-driven case is still to be found. The third point here concerns the feature that the work shows, numerically and analytically, clear core and wall-layer responses as might be expected but there is a very significant corner vortex as well. This plays a much more important role in the present nonsymmetric scenario because of its influence on the mass-flux balance and on the appearance of flow reversal, than it does in the symmetric case. Finally, most of the investigation has been for steady motions, but to help potentially in terms of improving the application we have extended the theory to cover unsteady flows, nonsymmetric incident motion and the extra effects due to certain basic shapes of daughter vessels.

We re-emphasize that our central concern has been with the theoretical/analytical issues emerging as fundamental to the understanding of the 3D branching flows. The generalization to any cross-sectional shape of vessels exists in terms of the intricate

flow structure and the related logarithmic effects that arise in the mass flux in each daughter vessel, for example. Increased relevance to physiological flows may follow in future work.

Additionally, we observe that although the asymptotic analysis applied in the study tends to work quite well in terms of comparisons with the numerical solutions at the above Reynolds numbers for some quantities (such as the wall-shear stress, the overall mass flux and in some sense other bulk properties), not all the fine structure is necessarily evident at such medium effective flow rates. Nonetheless, the so-called universal formula may prove to be useful, the qualitative physical insight may help, and the work may provide a test case for further explorations. Experimental studies of this quite basic 3D branching with nonsymmetry would be of considerable interest. The present study also potentially opens the way to 3D network applications.

Acknowledgements

Appendix A. The wall-layer solution downstream in the pressure-driven cases

The axial velocity perturbation U in the viscous wall layer must decay as $-p_\infty/N$ at large N, far downstream, in view of the flow structure in the main text. The reason is that the balances of continuity and azimuthal momentum imply $U_{xx} \sim P_{xx}/N$ at large N, following which a double integration in x (given zero disturbances far upstream) establishes the decay result far downstream with p_∞ being the imposed pressure value in the daughter vessel downstream. On the other hand, the typical N-scale expands like $x^{1/3}$ then. For large x, the corresponding wall-layer response is therefore found to take on a similarity form in which $U \sim x^{1/3} f(\eta)$ with $\eta = N/x^{1/3}$ and where the azimuthal velocity component $W_1 = O(x^{-4/3})$ and is proportional to s, while V_1 is identically zero. Thus U is independent of s and the downstream structure leads to requiring that the function $f(\eta)$ satisfies

$$f'' + \tfrac{1}{3}\eta^2 f' + \tfrac{1}{3}\eta f = 0, \tag{A.1}$$

subject to $f(0) = 0$ and $f(\infty) = 0$. The behaviour at infinity, which is necessary for matching with the core flow, stems automatically from (A.1) with the latter indicating $1/\eta$ decay at large η.

A contour integral approach yields the following solution to (A.1) with two arbitrary constants $\mathcal{A}$, $\mathcal{B}$:

$$f(\eta) = \mathcal{A}\, e^{-\eta^3/9} \int_0^\infty e^{-r\eta^3} (1 + 9r)^{-2/3} r^{-2/3}\, dr + \mathcal{B} \int_{-1/9}^0 e^{q\eta^3} (1 + 9q)^{-2/3} |q|^{-2/3}\, dq.$$

Our boundary condition at $\eta = 0$ requires $\mathcal{A} = -\mathcal{B}$ whereas $f(\infty) = 0$ yields $\Gamma(1/3)\mathcal{B} = \overline{\Pi}$, where $f(\eta) \sim \overline{\Pi}\eta^{-1}$ for $\eta \gg 1$ and $\overline{\Pi} = \pm p_\infty$ is prescribed. Hence

$$f'(0) = \frac{\Gamma(2/3)}{3^{1/3}\Gamma(1/3)}\overline{\Pi} = (0.35047\cdots)\overline{\Pi},$$

determines the axial wall-shear-stress factor, in particular. Integration thus yields, after some manipulation, the result

$$\int_0^\eta f(\hat{\eta}) \, d\hat{\eta} \sim \frac{1}{3} \mathcal{B} \left\{ \begin{array}{l} 3\Gamma(1/3) \ln(\eta) - \Gamma(1/3)^2 \Gamma(2/3) \\[2mm] + \Gamma(1/3) \int_0^1 \frac{(1-m)^{-2/3} - 1}{m} \, dm \\[2mm] -3^{-2/3} \int_0^\infty e^{-q/9} \ln(q) q^{-2/3} \, dq \end{array} \right\},$$

at large η, and hence,

$$\int_0^\eta f(\hat{\eta}) \, d\hat{\eta} \sim \overline{\Pi}(\ln(\eta) + \overline{C_2})$$

for the axial mass flux far downstream, where $\overline{C_2} = -0.0461087$ to six significant figures. The finite part of this wall-layer contribution is small numerically; the majority of the flux is transported in the corner region.

References

[1]   C. K. Aidun and J. R. Clausen, "Lattice-Boltzmann method for complex flows", *Annu. Rev. Fluid Mech.* **42** (2010) 439–472; doi:10.1146/annurev-fluid-121108-145519.

[2]   R. Al-Shahi, J. S. Y. Fang, S. C. Lewis and C. P. Warlow, "Prevalence of adults with brain arteriovenous malformations: a community based study in Scotland using capture-recapture analysis", *J. Neurol. Neurosurg. Psychiatry* **73** (2002) 547–551; doi:10.1136/jnnp.73.5.547.

[3]   T. Alarcón, H. M. Byrne and P. K. Maini, "A design principle for vascular beds: the effects of complex blood rheology", *Microvascular Res.* **69** (2005) 156–172; doi:10.1016/j.mvr.2005.02.002.

[4]   A. D. Augst, B. Ariff, S. A. G. McG. Thom, X. Y. Xu and A. D. Hughes, "Analysis of complex flow and the relationship between blood pressure, wall shear stress, and intima-media thickness in the human carotid artery", *Am. J. Physiology-heart Circulatory Physiol.* **293** (2007) H1031–H1037; doi:10.1152/ajpheart.00989.2006.

[5]   S. Balta and F. T. Smith, "Inviscid and low-viscosity flows in multi-branching and reconnecting networks", *J. Engrg. Math.* **104** (2017) 1–18; doi:10.1007/s10665-016-9869-3.

[6]   J. Bennett, "Theoretical properties of three-dimensional interactive boundary-layers". Ph. D. Thesis, University College London, 1987.

[7]   P. L. Bhatnagar, E. P. Gross and M. Krook, "A model for collision processes in gases. I. Small amplitude processes in charged and neutral one-component systems", *Phys. Rev.* **94** (1954) 511; doi:10.1103/PhysRev.94.511.

[8]   M. G. Blyth and A. J. Mestel, "Steady flow in a dividing pipe", *J. Fluid Mech.* **401** (1999) 339–364; doi:10.1017/S0022112099006904.

[9]   R. I. Bowles, S. C. R. Dennis, R. Purvis and F. T. Smith, "Multi-branching flows from one mother tube to many daughters or to a network", *Philos. Trans. R. Soc. Lond. A Math. Phys. Engrg. Sci.* **363** (2005) 1045–1055; doi:10.1098/rsta.2005.1548.

[10] R. I. Bowles, N. C. Ovenden and F. T. Smith, "Multi-branching three-dimensional flow with substantial changes in vessel shapes", *J. Fluid Mech.* **614** (2008) 329–354; doi:10.1017/S0022112008003522.

[11] K. J. Cassidy, N. Gavriely and J. B. Grotberg, "Liquid plug flow in straight and bifurcating tubes", *J. Biomech Engrg.* **123** (2001) 580–589; doi:10.1115/1.1406949.

[12] S. Chen and G. D. Doolen, "Lattice Boltzmann method for fluid flows", *Annu. Rev. Fluid Mech.* **30** (1998) 329–364; doi:10.1146/annurev.fluid.30.1.329.

[13] J. K. Comer, C. Kleinstreuer and Z. Zhang, "Flow structures and particle deposition patterns in double-bifurcation airway models. Part 1. Air flow fields", *J. Fluid Mech.* **435** (2001) 25–54; doi:10.1017/S0022112001003809.

[14] N. S. Denisenko et al., "Experimental measurements and visualisation of a viscous fluid flow in y-branching modelling the common carotid artery bifurcation with mr and doppler ultrasound velocimetry", *J. Phys.: Conf. Ser.* **722** (2016) 012013; doi:10.1088/1742-6596/722/1/012013.

[15] O. A. El-Masry, I. A. Feuerstein and G. F. Round, "Experimental evaluation of streamline patterns and separated flows in a series of branching vessels with implications for atherosclerosis and thrombosis", *Circ. Res.* **43** (1978) 608–618; doi:10.1161/01.RES.43.4.608.

[16] L. Formaggia, D. Lamponi and A. Quarteroni, "One-dimensional models for blood flow in arteries", *J. Engrg. Math.* **47** (2003) 251–276; doi:10.1023/B:ENGI.0000007980.01347.29.

[17] J. E. F. Green, F. T. Smith and N. C. Ovenden, "Flow in a multi-branching vessel with compliant walls", *J. Engrg. Math.* **64** (2009) 353–365; doi:10.1007/s10665-009-9285-z.

[18] Z. Guo, C. Zheng and B. Shi, "An extrapolation method for boundary conditions in lattice boltzmann method", *Phys. Fluids* **14** (2002) 2007–2010; doi:10.1063/1.1471914.

[19] G. J. Hademenos, T. F. Massoud and F. Viñuela, "A biomathematical model of intracranial arteriovenous malformations based on electrical network analysis: theory and hemodynamics", *Neurosurgery* **38** (1996) 1005–1015; doi:10.1097/00006123-199605000-00030.

[20] X. He and L.-S. Luo, "Lattice Boltzmann model for the incompressible Navier–Stokes equation", *J. Stat. Phys.* **88** (1997) 927–944; doi:10.1023/B:JOSS.0000015179.12689.e4.

[21] T. Inamuro, M. Yoshino and F. Ogino, "A non-slip boundary condition for lattice Boltzmann simulations", *Phys. Fluids* **7** (1995) 2928–2930; doi:10.1063/1.868766.

[22] A. W. McEvoy, N. D. Kitchen and D. G. T. Thomas, "Intracerebral haemorrhage in young adults: the emerging importance of drug misuse", *Br. Med. J.* **320** (2000) 1322; doi:10.1136/bmj.320.7245.1322.

[23] M. S. Olufsen, C. S. Peskin, W. Y. Kim, E. M. Pedersen, A. Nadim and J. Larsen, "Numerical simulation and experimental validation of blood flow in arteries with structured-tree outflow conditions", *Ann. Biomed. Engrg.* **28** (2000) 1281–1299; doi:10.1114/1.1326031.

[24] N. C. Ovenden, F. T. Smith and G. X. Wu, "The effects of nonsymmetry in a branching flow network", *J. Engrg. Math.* **63** (2009) 213–239; doi:10.1007/s10665-008-9232-4.

[25] T. J. Pedley, "Mathematical modelling of arterial fluid dynamics", *J. Engrg. Math.* **47** (2003) 419–444; doi:10.1023/B:ENGI.0000007978.33352.59.

[26] O. Pranevicius, M. Pranevicius and D. S. Liebeskind, "Partial aortic occlusion and cerebral venous steal: venous effects of arterial manipulation in acute stroke", *Stroke* **42** (2011) 1478–1481; doi:10.1161/STROKEAHA.110.603852.

[27] A. R. Pries and T. W. Secomb, "Modeling structural adaptation of microcirculation", *Microcirculation* **15** (2008) 753–764; doi:10.1080/10739680802229076.

[28] N. Resnick, S. Einav, L. Chen-Konak, M. Zilberman, H. Yahav and A. Shay-Salit, "Hemodynamic forces as a stimulus for arteriogenesis", *Endothelium* **10** (2003) 197–206; doi:10.1080/10623320390246289.

[29] R. Rieu and R. Pelissier, "In vitro study of a physiological type flow in a bifurcated vascular prosthesis", *J. Biomech.* **24** (1991) 923–933; doi:10.1016/0021-9290(91)90170-R.

[30] T. W. Secomb and A. R. Pries, "Basic principles of hemodynamics", in: *Handbook of hemorheology and hemodynamics* (IOS Press, Amsterdam, 2007) 289–306.

[31] F. T. Smith, "Steady motion through a branching tube", *Proc. R. Soc. Lond. Ser. A Math. Phys. Engrg. Sci.* **355** (1977) 167–187; doi:10.1098/rspa.1977.0093.

[32] F. T. Smith, "On internal fluid dynamics", *Bull. Math. Sci.* **2** (2012) 125–180; doi:10.1007/s13373-012-0019-6.

[33] F. T. Smith and M. A. Jones, "One-to-few and one-to-many branching tube flows", *J. Fluid Mech.* **423** (2000) 1–31; doi:10.1017/S0022112000002019.

[34] F. T. Smith and M. A. Jones, "AVM modelling by multi-branching tube flow: large flow rates and dual solutions", *Math. Med. Biol.* **20** (2003) 183–204; doi:10.1093/imammb/20.2.183.

[35] F. T. Smith, N. C. Ovenden, P. T. Franke and D. J. Doorly, "What happens to pressure when a flow enters a side branch?", *J. Fluid Mech.* **479** (2003) 231–258; doi:10.1017/S002211200200366X.

[36] F. T. Smith, R. Purvis, S. C. R. Dennis, M. A. Jones, N. C. Ovenden and M. Tadjfar, "Fluid flow through various branching tubes", *J. Engrg. Math.* **47** (2003) 277–298; doi:10.1023/B:ENGI.0000007981.46608.73.

[37] M. Tadjfar and F. T. Smith, "Direct simulations and modelling of basic three-dimensional bifurcating tube flows", *J. Fluid Mech.* **519** (2004) 1–32; doi:10.1017/S0022112004000606.

[38] O. R. Tutty, "Flow in a tube with a small side branch", *J. Fluid Mech.* **191** (1988) 79–109; doi:10.1017/S0022112088001521.

[39] A. H. White and F. T. Smith, "Computational modelling of the embolization process for the treatment of arteriovenous malformations (AVMs)", *Math. Comput. Model.* **57** (2013) 1312–1324; doi:10.1016/j.mcm.2012.10.033.

[40] F. Wilquem and G. Degrez, "Numerical modeling of steady inspiratory airflow through a three-generation model of the human central airways", *J. Biomech. Engrg.* **119** (1997) 59–65; doi:10.1115/1.2796065.

[41] D. A. Wolf-Gladrow, *Lattice-gas cellular automata and lattice Boltzmann models: an introduction* (Springer, Heidelberg, 2000); doi:10.1007/b72010.

[42] K. Yokoi, F. Xiao, H. Liu and K. Fukasaku, "Three-dimensional numerical simulation of flows with complex geometries in a regular cartesian grid and its application to blood flow in cerebral artery with multiple aneurysms", *J. Comput. Phys.* **202** (2005) 1–19; doi:10.1016/j.jcp.2004.06.018.